EARTHQUAKE ENGINEERING AND STRUCTURAL DYNAMICS
*Earthquake Engng Struct. Dyn.* 2011; **40**:1241–1261
Published online 18 January 2011 in Wiley Online Library (wileyonlinelibrary.com). DOI: 10.1002/eqe.1086

# Seismic design and shake table tests of a steel post-tensioned self-centering moment frame with a slab accommodating frame expansion

Chung-Che Chou[1,2,*,†,‡,§] and Jun-Hen Chen[2,3,¶]

[1]*Department of Civil Engineering, National Taiwan University, Taiwan*
[2]*National Center for Research on Earthquake Engineering, Taiwan*
[3]*Department of Civil Engineering, National Chiao Tung University, Hsinchu, Taiwan*

## SUMMARY

Post-tensioned (PT) self-centering moment frames were developed as an alternative to welded moment-resisting frames (MRFs). Lateral deformation of a PT frame opens gaps between beams and columns. The use of a composite slab in welded MRFs limits the opening of gaps at the beam-to-column interfaces but cannot be adopted in PT self-centering frames. In this study, a sliding slab is used to minimize restraints to the expansion of the PT frame. A composite slab is rigidly connected to the beams in a single bay of the PT frame. A sliding device is installed between the floor beams and the beams in other bays, wherever the slab is allowed to slide. Many shaking table tests were conducted on a reduced-scale, two-by-two bay one-story specimen, which comprised one PT frame and two gravitational frames (GFs). The PT frame and GFs were self-centering throughout the tests, responding in phase with only minor differences in peak drifts that were caused by the expansion of the PT frame. When the specimen was excited by the 1999 Chi-Chi earthquake with a peak ground acceleration of 1.87*g*, the maximum interstory drift was 7.2% and the maximum lateral force was 270 kN, equal to 2.2 times the yield force of the specimen. Buckling of the beam bottom flange was observed near the column face, and the initial post-tensioning force in the columns and beams decreased by 50 and 22%, respectively. However, the specimen remained self-centering and its residual drift was 0.01%. Copyright © 2011 John Wiley & Sons, Ltd.

Received 11 October 2009; Revised 22 October 2010; Accepted 23 October 2010

KEY WORDS: post-tensioned frame; frame expansion; slab sliding; shake table tests

## INTRODUCTION

A post-tensioned (PT) self-centering moment frame that uses post-tensioning steel to compress steel beams against columns was developed as an alternative to the steel welded moment-resisting frame (MRF). Lateral deformation of a PT frame opens gaps at the beam-to-column interfaces (Figure 1(a)). Both the elastic responses of strands and the hysteretic responses of energy-dissipating devices produce a flag-shaped hysteretic behavior of the connection (Figure 1(b)). Many researchers have experimentally validated the self-centering behaviors of PT connections and columns with either energy yielding or friction-damped devices [1–11]. Analytical studies also show that in terms of maximum interstory drift and residual drift, the seismic performance

*Correspondence to: Chung-Che Chou, Department of Civil Engineering, National Taiwan University, Taiwan.
†E-mail: cechou@ntu.edu.tw
‡Associate Professor.
§Associate Research Fellow.
¶Graduate Student Researcher.

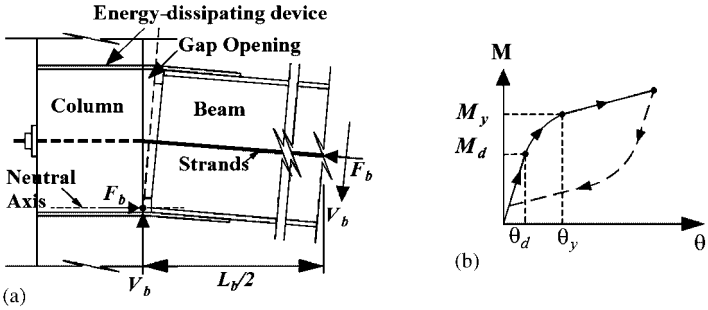


Figure 1. (a) PT connection and (b) flag-shaped hysteretic behavior.

of an MRF with PT connections exceeds the performance of an MRF with typical welded connections [12, 13].

Although the newly developed PT connection provides satisfactory cyclic performance, Kim and Christopoulos [13] and Garlock *et al.* [14, 15] raised the issue of how columns and slabs restrainted PT frame expansion. Gap opening at the beam-to-column interfaces causes an expansion of the PT frame. The column and slab restraints that oppose the frame expansion affect the compression force in the PT beam. Kim and Christopoulos [13] suggested an approximate approach to estimate the restraint, which is appropriate in cases where a more concentrated response occurs at a single floor alone and overly conservative in cases where the structure responds in its fundamental mode. For a PT frame that responds in its fundamental mode, Chou and Chen [16] proposed a method for evaluating the restraint that considered the continuity and boundary conditions of the column. The method requires a structural analysis of the column in a deformed configuration and equations that are derived from the compatibility of deformation of beams, strands, and columns.

When gaps open at the beam-to-column interfaces, the concrete slab, if it does not open near the columns, restrains frame expansion, affecting the self-centering [17]. Garlock *et al.* [14, 15] and King [10] suggested that the collector beams or bays transfer the inertial force into the PT frame and accommodate PT frame expansion. Kim and Christopoulos [13] proposed details along the boundaries of the slabs that allow for the gap openings to be accommodated. More recently, Chou *et al.* [18] experimentally showed that the PT connection with a continuous composite slab self-centers with low residual deformations as long as the metal deck separates near the column and the negative connection moment provided by slab reinforcement is considered in design. Chou *et al.* [19] also demonstrated similar cyclic responses between a bare PT connection and a composite PT connection with a fully discontinuous composite slab, which opens freely along with the gap opening at the beam-to-column interface.

The aforementioned slab [18, 19], which enables the opening of gaps to be accommodated along the slab boundaries, is composed of concrete, separate metal decks, and unbonded (or separate) longitudinal bars near the face of the column, making construction more difficult than that of the MRF. An alternative method, proposed by Garlock *et al.* [14] and King [10], is experimentally verified herein by rigidly connecting the slab to the beam in a single bay of the PT frame to transfer lateral forces, and by placing the slab on other beams to permit relative lateral translation. To allow a smooth sliding motion between the PT frame and the GFs, Teflon pads are placed underneath the floor beams at the sides where sliding of the slab is expected. In this study, the mechanics of PT self-centering frames using the slab details are described first. A procedure for designing a PT frame that is adapted from the current seismic design practices for a PT frame with the slab details is then presented. A three-story building, incorporating PT frames and GFs, is designed and modeled numerically to investigate its pushover response. Many shake table tests are conducted on a reduced-scale, two-by-two bay one-story PT building structure. The objectives of the test program are to determine (1) how the slab restrains frame expansion, (2) the seismic responses of a PT frame and GFs, and (3) the variation of compression forces in PT beams.



DOI: 10.1002/eqe

## DESIGN OF PROTOTYPE STRUCTURE

Figure 2(a) and (b) shows the plan and elevation of the prototype building. Three two-bay PT frames that provide lateral load resistance in the east–west direction are considered in this study; each prototype PT frame is composed of three PT concrete-filled tube (CFT) columns and six PT steel beams. Reduced flange plates (RFPs) proposed in the prior studies [4, 18, 20] are incorporated at each beam-to-column connection to increase energy dissipation (Figure 2(c)), and no energy dissipation device is provided at the base of the column (Figure 2(d)). Shear studs are used on

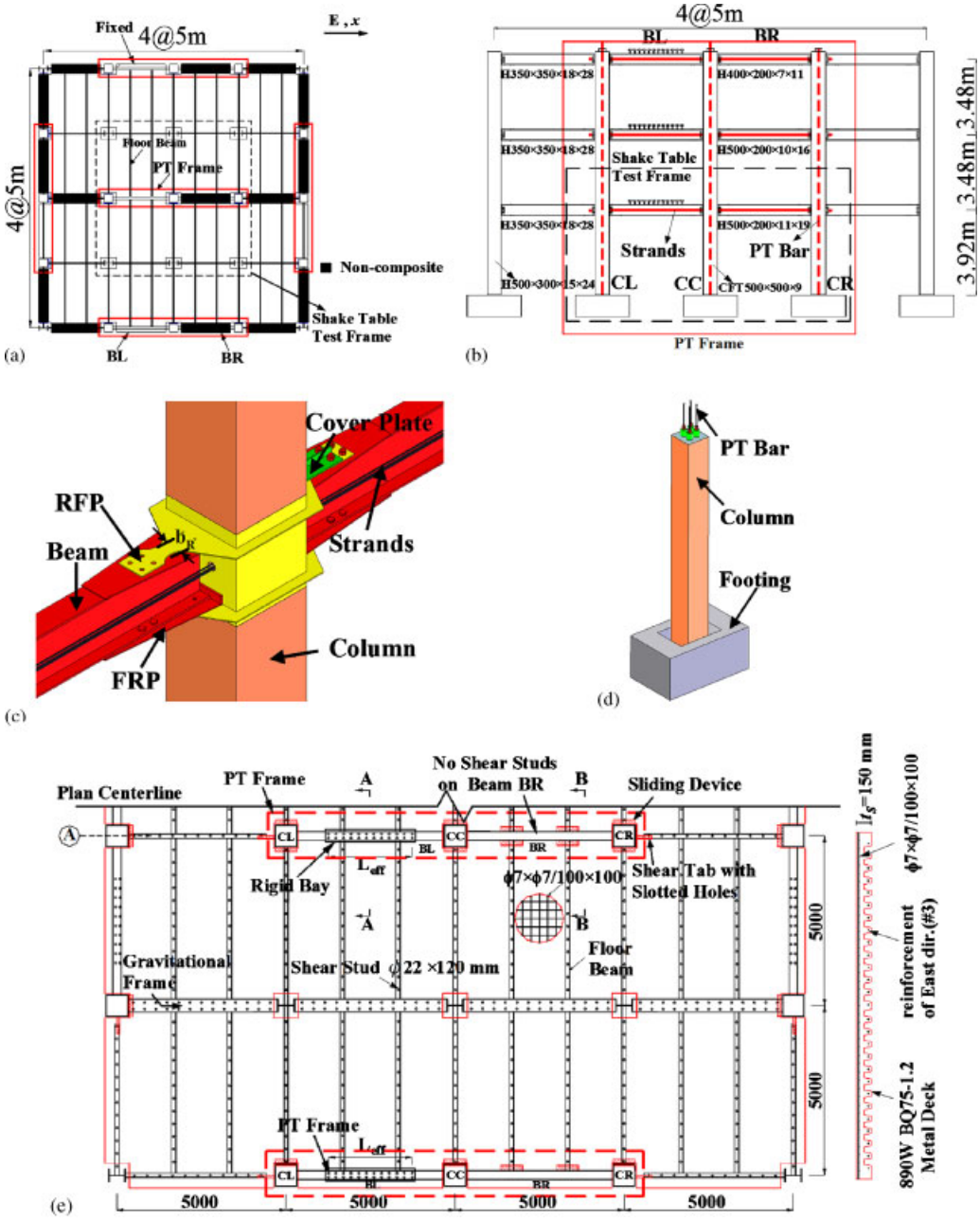


Figure 2. Prototype properties: (a) plan; (b) elevation; (c) PT connection; (d) PT column; (e) slab details; (f) view A-A; (g) view B-B; (h) sliding device; (i) pushover curve; and (j) slab free-body diagram.



DOI: 10.1002/eqe

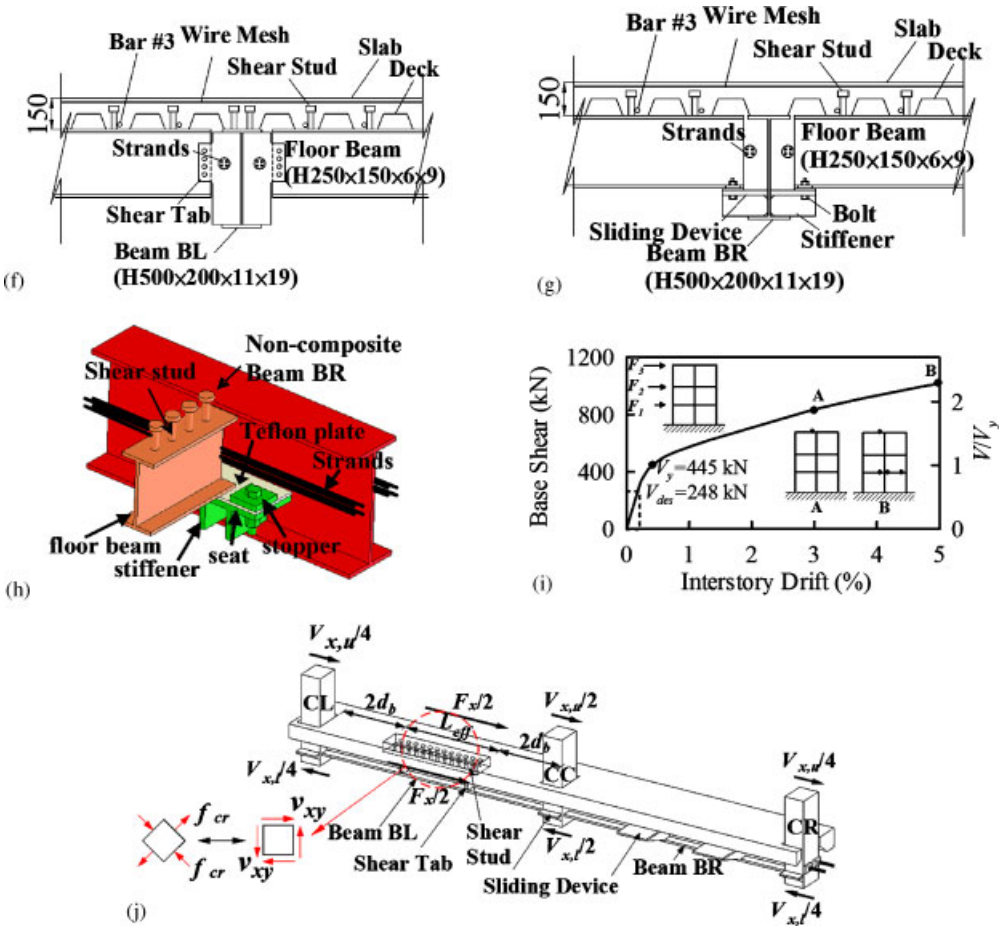


Figure 2. *Continued.*

the top of each floor beam to form a full composite section between the slab and floor beam (Figure 2(e)). To eliminate slab restraints to the expansion of the PT frame, the slab is rigidly connected to the beam BL in one bay of the PT frame with shear studs (Figure 2(e) and (f)) and placed on the top of another beam along line A (Figure 2(e) and (g)). A shear tab extending over the beam flange width is bolted to the web of the floor beam (Figure 2(f)). A rigid bay is detailed such that the shear strength of studs or concrete is larger than the inertial force. Gap opening is unrestricted because the beams along line A can slide on the sides where the floor beam is simply supported by a sliding device. The device, which is composed of a low-friction Teflon plate between the floor beam and a steel seat (Figure 2(h)), is positioned on both sides of the columns and beams along line A. The steel seat is a flat plate, vertically reinforced by several stiffeners. The flat plate and stiffeners are welded to the beam bottom side. The device, which does not have a slotted hole to decrease its flexural stiffness, differs from that proposed by Garlock *et al.* [14] or King [10]. The device is designed to support the dead load and live load transferred from one end of the floor beam. The necessary travel of the floor beam on the sliding device is limited by stoppers. A gap is provided between the floor beam and the stopper (Figure 2(h)) and also between the PT columns and the slab to exclude contact at a drift of 5%. Although the ribs of the metal deck and longitudinal reinforcement are continuous through the column lines, the PT frame can expand without restraints provided by the slab. For example, when the GF moves laterally $\Delta_d$ (Figure 3(a)), the PT frame moves $\Delta_d$ and further expands $\Delta$ due to the gap openings at the beam-to-column interfaces. The span in the PT frame increases from the original length $L_c$ to $L_c+2\Delta$, while that in the GF remains $L_c$.



DOI: 10.1002/eqe

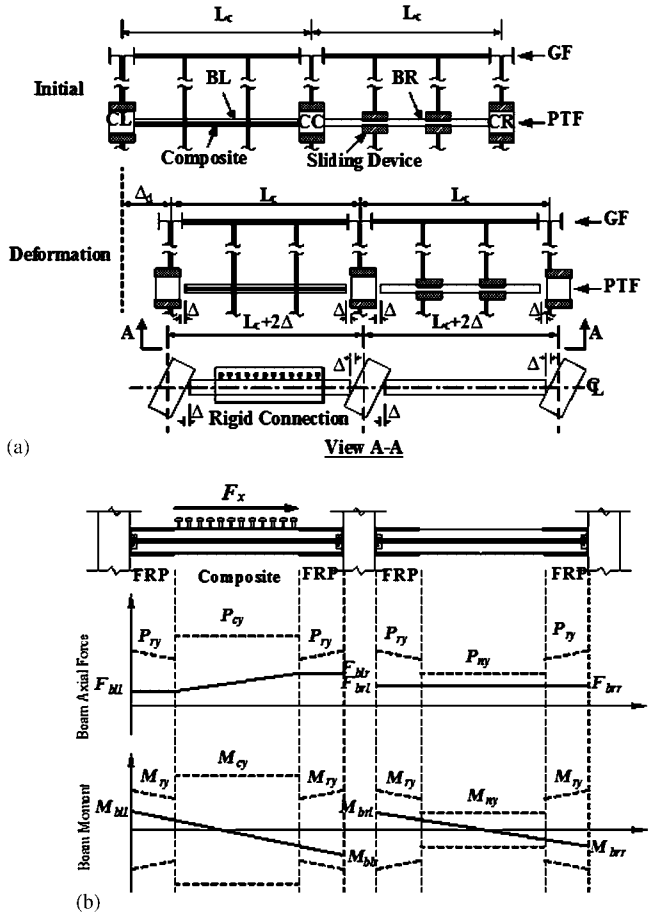


(Note: $P_{ry}$ and $M_{ry}$ are the axial and flexural yield capacities including flange reinforcing plates
$P_{cy}$ and $M_{cy}$ are the axial and flexural yield capacities in the full-composite beam section)

Figure 3. Frame deformation and force variation in the beams: (a) frame deformation and (b) force and moment in the beams.

A procedure proposed by Garlock *et al.* [15] is adopted to design a PT prototype frame. The design dead loads are 5.28 kPa (110 psf) and 4.32 kPa (90 psf) for the floors and the roof, whereas the live loads for the floors and the roof are 2.39 kPa (50 psf), resulting in a total seismic weight of the building equal to 5952 kN. The design details follow the work by Chou and Chen [16, 21] using a force reduction factor $R$ of 8, an overstrength $\Omega_0$ of 3 and a deflection amplification factor $C_d$ of 5.5. The structural period $T$ and the seismic response coefficient $C_s$ calculated by the codified method are 0.6 s and 0.125, respectively, so the seismic design base shear $V_{des}$ for one PT frame is 248 kN.

*Beam and column sizes*

The selected beam and column sizes, RFP thickness, $t_R$, and narrowest dimension, $b_R$ (Figure 2(c)), strand and PT bar areas, $A_{ST}$, and initial PT force, $T_{in}$, are given in Table I(a) and (b). The $500 \times 500$ mm CFT column with 9-mm-thick tube contains four 36-mm-diameter ASTM A416 Grade 270 PT bars. The specified 28-day concrete strength is 28 MPa, and the ASTM A572 Grade 345 (50) steel is used for the steel beams. The ASTM A416 Grade 270 strands are passed along the beam web and anchored outside the exterior columns.

Figure 4(a) shows the free-body diagram of a typical story. The steel beam is connected to the slab via shear studs to transfer a lateral force, $F_x$, from the slab to the frame. The compression force



DOI: 10.1002/eqe

Table I. Prototype properties: (a) beam and column sizes; (b) PT element and RFP sizes; (c) connection moment; (d) stress ratios of the beam (3% drift); and (e) stress ratios of the beam (5% drift).

| Floor | Beam/column size | $F_x$ (kN) | $V_x$ (kN) | $\frac{F_{blr}}{P_{ny}}$ | $\frac{F_{brl}}{P_{ny}}$ | $\frac{M_E}{M_{ny}}$ | $\frac{M_D}{M_{ny}}$ | $\frac{M_L}{M_{ny}}$ | $\frac{F_{blr}}{P_{ny}}+\frac{M_{dem}}{M_{ny}}$ | $\frac{F_{brl}}{P_{ny}}+\frac{M_{dem}}{M_{ny}}$ |
|---|---|---|---|---|---|---|---|---|---|---|
| (a) | | | | | | | | | | |
| Third | H400 × 200 × 7 × 11 | 109 | 109 | 0.23 | 0.20 | 0.14 | 0.13 | 0.07 | 0.59 | 0.56 |
| Second | H500 × 200 × 10 × 16 | 91 | 200 | 0.18 | 0.17 | 0.20 | 0.09 | 0.04 | 0.53 | 0.52 |
| First | H500 × 200 × 11 × 19 | 48 | 248 | 0.21 | 0.20 | 0.27 | 0.08 | 0.03 | 0.61 | 0.60 |
| Column | CFT 500 × 500 × 9 | — | — | — | — | 0.24 | — | — | 0.24 | 0.24 |

| | PT element | | | RFP | | Flange reinforcing plate | |
|---|---|---|---|---|---|---|---|
| Floor | Number and size (mm Dia.) | $A_{ST}$ (mm$^2$) | $T_{in}$ (kN) | $t_R$ (mm) | $b_R$ (mm) | $t_p$ (mm) | $L_p$ (mm) |
| (b) | | | | | | | |
| Third | 6–15 | 790 | 500 | 6 | 120 | 5 | 800 |
| Second | 12–15 | 1579 | 650 | 8 | 120 | 8 | 1000 |
| First | 12–15 | 1579 | 900 | 10 | 120 | 9 | 1000 |
| Column | 4–36 | 4072 | 1100 | — | — | — | — |

| Floor | $\frac{M_d}{M_{np}}$ | $\frac{M_{dem}}{M_{np}}$ | $\frac{M_y}{M_{np}}$ | $\frac{M_{dem}}{M_d}$ | $\frac{M_{dem}}{M_y}$ | $\alpha$ | $\beta$ | $\alpha_y$ |
|---|---|---|---|---|---|---|---|---|
| (c) | | | | | | | | |
| Third | 0.30 | 0.36 | 0.46 | 1.2 | 0.8 | 0.10 | 1.0 | 1.29 |
| Second | 0.24 | 0.35 | 0.44 | 1.5 | 0.8 | 0.14 | 1.0 | 1.22 |
| First | 0.26 | 0.40 | 0.44 | 1.5 | 0.9 | 0.14 | 1.0 | 1.32 |
| Column | 0.25 | 0.24 | 0.25 | 1.0 | 1.0 | 0.07 | 0 | 1.06 |

| | | $\Delta F_b$ | | | Beam BL | | | Beam BR | | |
|---|---|---|---|---|---|---|---|---|---|---|
| Floor | $T_{in}$ (kN) | $\Delta T_{ST}$ (kN) | $\Delta F_{cc}$ (kN) | $F_x$ (kN) | $\frac{F_{blr}}{\phi_b P_{ry}}$ | $\frac{M_{blr}}{\phi_b M_{ry}}$ | $\sum$ | $\frac{F_{brl}}{\phi_b P_{ry}}$ | $\frac{M_{brl}}{\phi_b M_{ry}}$ | $\sum$ |
| (d) | | | | | | | | | | |
| Third | 500 | 132 | −1 | 360 | 0.27 | 0.67 | 0.94 | 0.22 | 0.45 | 0.67 |
| Second | 650 | 384 | −41 | 300 | 0.23 | 0.46 | 0.69 | 0.20 | 0.42 | 0.62 |
| First | 900 | 670 | 80 | 156 | 0.29 | 0.54 | 0.83 | 0.28 | 0.35 | 0.63 |
| (e) | | | | | | | | | | |
| Third | 500 | 264 | −2 | 548 | 0.37 | 0.81 | — | 0.32 | 0.55 | 0.83 |
| Second | 650 | 768 | −82 | 456 | 0.33 | 0.54 | 0.93 | 0.31 | 0.56 | 0.86 |
| First | 900 | 1440 | 160 | 237 | 0.47 | 0.69 | — | 0.46 | 0.58 | — |

*Note*: $M_{ny}$ is the flexural yield capacity of the beam or column; $P_{ny}$ is the axial yield capacity of the beam or column; $M_{np}$ is the nominal moment capacity of the beam or column.

in the beam BL is affected by the lateral force, the strand elongation, and the column restraint that opposes the frame expansion. Assuming that the story shear in the center column CC doubles that in the exterior column, the compression force on the left side of the beam BL, $F_{bll}$, is determined based on the horizontal force equilibrium of column CL (Figure 4(b))

$$F_{bll} = T_{in} + [\Delta T_{ST} + (\Delta F_{cc,u} + \Delta F_{cc,l})] - \left(\frac{V_{x,l}}{4} - \frac{V_{x,u}}{4}\right) + (T_{bll} - C_{bll})$$

$$= T_{in} + \Delta F_b - F_x/4 \tag{1}$$

where $\Delta F_b$ is the compression force increment due to the strand elongation ($\Delta T_{ST}$), the column restraint from an upper story ($\Delta F_{cc,u}$) and a lower story ($\Delta F_{cc,l}$); $V_{x,l}$ and $V_{x,u}$ are the story shears below and above the floor being considered, and$T_{bll}$ and $C_{bll}$ are the tensile and compressive forces in the RFPs, which are assumed to be the same. The compression force on the right



DOI: 10.1002/eqe

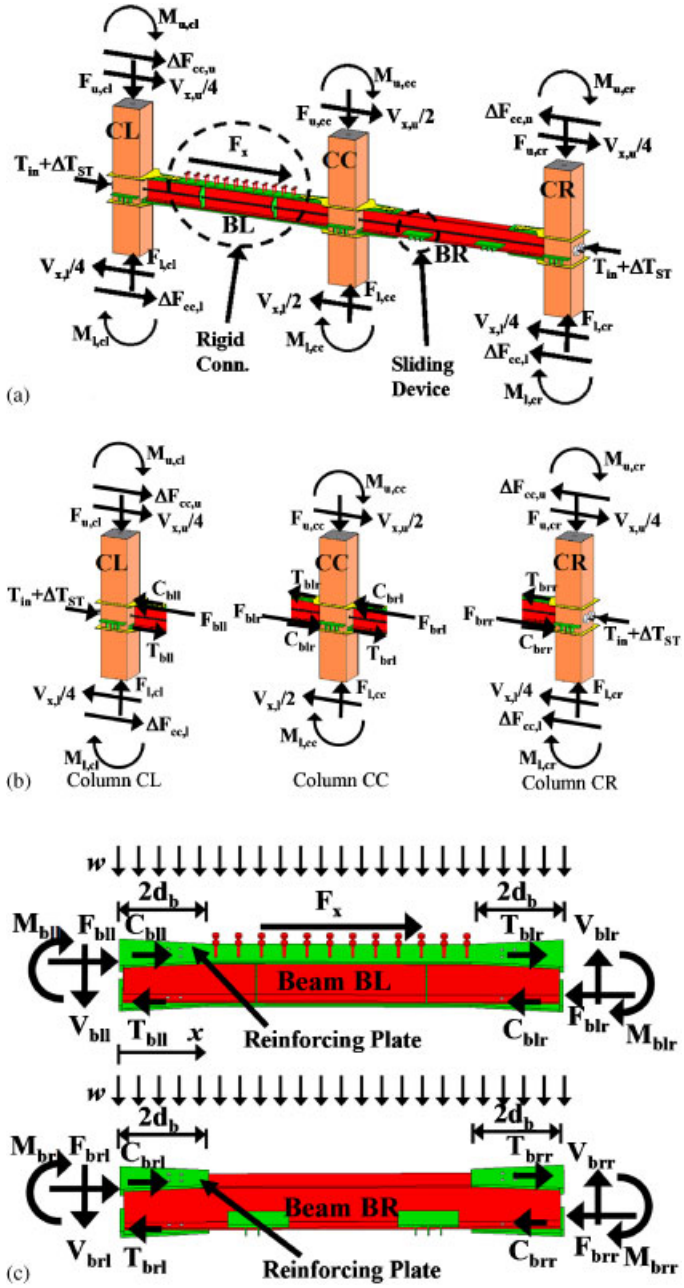


Figure 4. Free-body diagrams for columns and beams: (a) force distribution of PT frame; (b) column free-body diagram; and (c) beam free-body diagram.

side of the beam BL, $F_{blr}$, is determined based on the horizontal force equilibrium of beam BL (Figure 4(c))

$$F_{blr} = F_{bll} + F_x + (C_{bll} - T_{bll}) + (T_{blr} - C_{blr})$$

$$= T_{in} + \Delta F_b + 3F_x/4 \tag{2}$$

where $T_{blr}$ and $C_{blr}$ are the tensile and compressive forces in the RFPs welded to the center column CC. No shear connectors are adopted in the beam BR, so the compression force in the beam BR



DOI: 10.1002/eqe

is constant (i.e. $F_{brl} = F_{brr}$) and determined from the horizontal force equilibrium of column CC (Figure 4(b))

$$F_{brl} = F_{blr} - \left(\frac{V_{x,l}}{2} - \frac{V_{x,u}}{2}\right) + (C_{blr} - T_{blr}) + (T_{brl} - C_{brl})$$
$$= T_{in} + \Delta F_b + F_x/4 \tag{3}$$

where $T_{brl}$ and $C_{brl}$ are the tensile and compressive forces in the RFPs welded to the center column CC. Beam shear at the end of the beam, a contact point when the gap opens at the beam-to-column interface (Figure 1(a)), can be determined from the moment equilibrium in each beam (Figure 4(c)). Figure 3(b) shows the variation of compression force and bending moment in each beam. The dashed line represents the axial and flexural yield capacities of the beam, which increase with the width of the flange reinforcing plate (FRP) and are larger than the axial force and bending moment shown in solid lines.

Moment demands caused by the seismic design load ($M_E$), dead load ($M_D$), and live load ($M_L$) are given at the beam-to-column interface and the column base (Table I(a)). The moment $M_E$ is computed from the free-body diagram of the subassembly (Figure 4(b)), and the moments $M_D$ and $M_L$ are obtained from the structural analysis of the beam subjected to a uniformly distributed load $w$ (Figure 4(c)). The stress ratios in the beam BL, including axial load-bending moment interaction, are less than 1 (Figure 3(a)); these values at the column face are calculated as

$$\frac{F_{blr}}{P_{ny}} + \frac{M_{dem}}{M_{ny}} \tag{4}$$

where $P_{ny}$ is the axial yield capacity of the beam; $M_{ny}$ is the flexural yield capacity of the beam and $M_{dem}$ is $1.4M_D + 0.5M_L + M_E$. The same calculation is applied to the beam BR. The code-based design moment, $M_{dem}$, ranges between the decompression moment $M_d$ and the yield moment $M_y$ of the connection (Table I(c)). The decompression moment $M_d$ is composed of moments provided by the initial strand force ($M_{ST}$) and the RFPs ($M_R$), which is computed based on axial forces in the RFPs at the onset of gap opening and the distance between the top and bottom RFPs [16, 18]. No energy-dissipating device is provided at the base of the columns, so the code-based design moment is less than the decompression moment of the PT column ($T_{in} \times d_c/2$), where $d_c$ is the depth of the column.

*Reduced flange plate*

The connection moment at the onset of the RFP yielding is $M_y$, which is equal to $\alpha_y M_{dem}$, where $\alpha_y \geqslant 1.0$, indicating the elastic response of the PT frame under the code-based seismic load. The parameters $\alpha$ and $\beta$ for PT connections are listed in Table I(c), within the ranges ($0.1 \leqslant \alpha \leqslant 0.150, 0.7 \leqslant \beta \leqslant 1.0$) suggested by Kim and Christopoulos [13]. The parameter $\alpha$ was defined as a stiffness ratio of the PT connection between the post-yield stage and elastic stage. The parameter $\beta$ was defined as an energy dissipation ratio ($=2M_{R,3\%}/M_y$), where $M_{R,3\%}$ is the moment provided by the RFPs at a drift of 3%. At maximum considered earthquake (MCE) design level, the expected beam moment $M_b$ is 0.9–1.0$M_{np}$, and the moment provided by the RFPs is 0.2–0.3$M_{np}$, where $M_{np}$ is defined as the nominal moment capacity of the beam.

*Pushover curve of the PT frame*

Christopoulos *et al.* [2] proposed a rotational spring scheme to capture the self-centering response of PT connections. Chou and Chen [16, 21] utilized the same scheme with a modification in the way that the rotational spring in the connection and column base considers column restraints in a PT frame. This study used the rotational spring scheme to model the two-dimensional three-story prototype PT frame in the computer program PISA [22]. Beam-column elements were used to model beams and columns. Two zero-length spring elements connecting beam-column joints or column-footing joints were used to model the bilinear elastic behavior of the PT element and the



DOI: 10.1002/eqe

column restraint behavior, respectively. An additional spring element in beam-column joints was used to model the bilinear elastoplastic behavior of the RFP. The panel zone deformation, P-delta effects, and slab were not considered in the model. Detailed modeling technique for the three-story frame can be found elsewhere [16, 21]. The loading pattern defined in IBC 2000 [23] was adopted to obtain the pushover curve of the PT frame (Figure 2(i)). The normalized base shear was obtained by dividing the base shear by the value of $V_{des}=248\,\text{kN}$. The significant yield strength of the PT frame is $V_y=445\,\text{kN}$ ($1.79V_{des}$) at a roof drift of 0.4%. At a roof drift of 3 and 5%, the maximum base shear reaches $3.3V_{des}(1.9V_y)$ and $4.1V_{des}(2.3V_y)$; the corresponding lateral force at each floor, $F_x$, is listed in Table I(d) and (e). The axial forces in the beams BL and BR were calculated based on Equations (1)–(3), considering the effects of the column restraint ($\Delta F_{cc}$) and the strand elongation ($\Delta T_{ST}$) based on the previous work [16]. The stress ratios, including the axial force and bending moment at the column face, are less than 1 at an interstory drift of 3%. Beam yielding marked by a circle occurs in the third floor after reaching a drift of 3% (step A). Beams in the first floor also yields at a drift of 5% (step B). A blank in Table I(e) indicates a value larger than 1 at a 5% drift. Note that the stress ratio is larger in the beam BL than beam BR due to a lateral force $F_x$ applied to the beam BL.

*Concrete and shear stud strength*

A total of 24 shear studs (22 mm in diameter) were utilized in the beam BL (Figure 2(e)) to develop full-composite action. The shear strength of studs calculated based on the AISC Specification for Structural Steel Buildings (AISC-LRFD) [24] is 3790 kN, much larger than the lateral force $F_x$ at a drift of 5% (Table I(e)). Based on the assumption that the slab is subjected to pure shear under a lateral force (Figure 2(j)), the concrete cracking capacity under shear, $V_{cr}$, is determined from the concrete tensile strength [25] times the effective slab area

$$V_{cr}=0.33\sqrt{f_c'}\left(\tfrac{3}{4}t_s L_{eff}\right) \tag{5}$$

where $t_s$ is the slab thickness; $L_{eff}$ is the effective slab length, where all shear studs are welded to the beam, and $f_c'$ is the specified concrete strength (28 MPa). In an exterior PT frame, the effective slab length is 2.5 m in the bottom two floors and 2.9 m in the third floor; the slab thickness is 150 mm. The concrete shear capacity at cracking calculated based on Equation (5) is 490 kN for the bottom two floors and 570 kN for the third floor, which are larger than the lateral force $F_x$ at a drift of 5% (Table I(e)). Therefore, the slab could transfer the inertia force into the exterior PT frame. Note that in more realistic situation in which more bays are arranged as gravity frames, the shear capacity of the slab might not be able to carry the lateral force so a combination of the heaviest gauge steel decking with the thickest concrete and an underlying system of truss-like members might be another method [10, 14].

## CONSTRUCTION OF SPECIMEN MODEL AND EXPERIMENTAL ARRANGEMENT

Figure 5(a) shows the elevation of the specimen and experimental set-up. The specimen comprises a two-bay by first-story interior PT frame and two exterior GFs. A scale model of the PT building structure on the shaking table cannot have a ratio of larger than 1:2.5, so the length and mass scale factors are $S_L=0.4$ and $S_L^2=0.16$, respectively. Table II shows the scaling ratios for the sectional modulus $S$, size and force associated with the structural members. The scaling ratios for the floor beam and slab are larger than required because the smallest beams and metal decks available in Taiwan are larger than required. Figure 5(b) shows that the top of the sliding device has a 5-mm-thick Teflon plate, whose friction coefficient, according to the manufacturer, is 0.025. The friction force, estimated from the reaction of the floor beam, was 0.2 kN much less than the lateral force in the floor. The gap between the floor beam and the stopper was 20 mm, which was larger than the expansion of the PT frame (=16 mm) at a 5% drift.

A total of 24 shear studs (13 mm in diameter) were utilized in the beam BL to develop full-composite section. The effective slab length, $L_{eff}$, and thickness, $t_s$, were 950 and 80 mm,



DOI: 10.1002/eqe

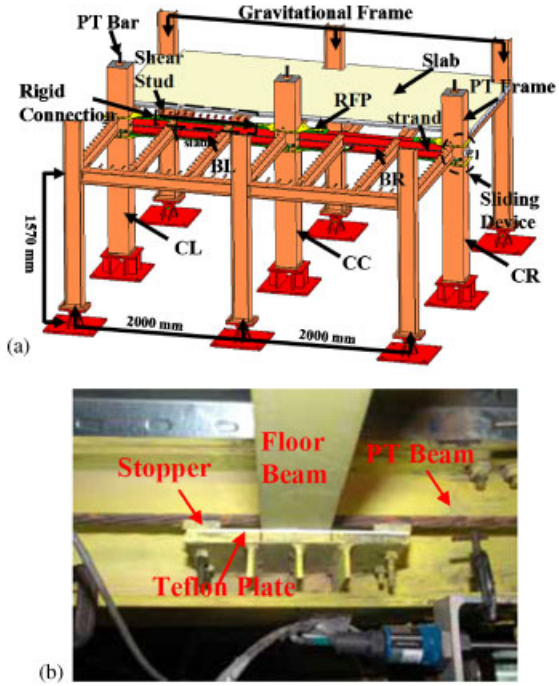


Figure 5. Overall view of the specimen and sliding device: (a) specimen and (b) sliding device.

Table II. Scaled specimen properties: (a) member size; (b) PT elements; and (c) RFP and slab sizes.

| | | Prototype | | Specimen | | Scale ratio |
|---|---|---|---|---|---|---|
| Frame | | Member size | $S$ (cm$^3$) | Member size | $S$ (cm$^3$) | ($S_L^3 = 0.064$) |
| (a) | | | | | | |
| PT frame | Column | CFT500 × 500 × 9 | 3255 | CFT 250 × 250 × 4 | 289 | 0.089 |
| | Beam | H500 × 200 × 11 × 19 | 2234 | H200 × 100 × 5.5 × 8 | 139 | 0.062 |
| Gravitational frame | Column | H500 × 300 × 15 × 24 | 3883 | H250 × 150 × 6 × 9 | 277 | 0.071 |
| | Beam | H350 × 350 × 18 × 28 | 3429 | H150 × 150 × 7 × 10 | 219 | 0.064 |
| | Floor beam | H250 × 150 × 6 × 9 | 324 | H150 × 75 × 5 × 7 | 89 | 0.275 |

| | Prototype | | Specimen | | Scale ratio ($S_L^2 = 0.16$) | |
|---|---|---|---|---|---|---|
| Member | $A_{rea}$ (mm$^2$) | $T_{in}$ (kN) | $A_{rea}$ (mm$^2$) | $T_{in}$ (kN) | $A_{rea}$ | $T_{in}$ |
| (b) | | | | | | |
| Column | 4072 | 1100 | 652 | 176 | 0.13 | 0.16 |
| Beam | 1579 | 900 | 253 | 144 | 0.17 | 0.16 |

| RFP size | Prototype | Specimen | Scale ratio | Slab size | Prototype | Specimen | Scale ratio |
|---|---|---|---|---|---|---|---|
| (c) | | | | | | | |
| Length (mm) | 540 | 317 | 0.59 | Span (mm) | 5000 | 2000 | 0.4 |
| Width (mm) | 120 | 40 | 0.33 | Thickness (mm) | 150 | 80 | 0.53 |
| Thickness (mm) | 8 | 4 | 0.5 | Bar area (mm$^2$) | 127 | 71 | 0.59 |
| Reduced sectional area (mm$^2$) | 960 | 200 | 0.21 | Mesh area (mm$^2$) | 71 | 12.6 | 0.18 |

respectively. The concrete shear capacity at cracking calculated based on Equation (5) was 132 kN for one side of the slab; the lateral force in the slab that was transferred into the beam BL without shear cracks was 264 kN, which was more than six times the lateral force ($S_L^2 V_{des} = 40$ kN).



DOI: 10.1002/eqe

Table III. Test program.

| Earthquake | Station | Sequence | Scaled ratio | PGA ($g$) | Maximum drift (%) | Floor acceleration ($g$) | Base shear (kN) | Failure mode |
|---|---|---|---|---|---|---|---|---|
| (*a*) *Phase I* | | | | | | | | |
| | | | Phase I ($T=0.16$ s, $m=9480$ kg) | | | | | |
| 1994 Northridge (PGA=0.47$g$) | CNP196 Canoga Park ($S_a=1.40g$) ($mS_a=130$ kN) | 1 | 0.11 | 0.05 | 0.1 | 0.07 | 7 | — |
| | | 2 | 0.80 | 0.38 | 0.3 | 0.90 | 84 | — |
| | | 7 | 1.98 | 0.93 | 0.8 | 1.39 | 129 | Column CC slip |
| | | 8 | 3.36 | 1.58 | 1.6 | 1.97 | 183 | — |
| | | 9 | 5 | 2.35 | 2.1 | 2.01 | 187 | — |
| 1999 Chi-Chi (PGA=0.38$g$) | TCU074 ($S_a=$ 0.83$g$)($mS_a=$ 77 kN) | 3 | 0.13 | 0.05 | 0.1 | 0.06 | 5 | — |
| | | 4 | 0.53 | 0.20 | 0.1 | 0.28 | 26 | — |
| | | 5 | 1.31 | 0.50 | 0.2 | 0.41 | 38 | — |
| | | 6 | 1.39 | 0.53 | 0.3 | 0.80 | 74 | — |
| (*b*) *Phase II* | | | | | | | | |
| | | | Phase I ($T=0.18$ s, $m=12\,640$ kg) | | | | | |
| 1994 Northridge (PGA= 0.47$g$) | CNP196 Canoga Park ($S_a=1.32g$) ($mS_a=164$ kN) | 3 | 1.38 | 1.65 | 0.5 | 0.92 | 115 | — |
| | | 4 | 2.36 | 1.11 | 1.6 | 1.19 | 147 | — |
| | | 5 | 2.45 | 1.15 | 1.8 | 1.31 | 163 | — |
| | | 7 | 4.28 | 2.01 | 4.2 | 1.82 | 226 | Two RFP fracture |
| | | — | — | — | — | — | — | — |
| 1999 Chi-Chi (PGA= 0.38$g$) | TCU074 $S_a=$ 0.83$g$)($mS_a=$ 102 kN) | 1 | 1.29 | 0.49 | 0.5 | 0.86 | 106 | — |
| | | 2 | 3.92 | 1.49 | 2.1 | 1.56 | 193 | — |
| | | 6 | 5.08 | 1.97 | 3.9 | 1.92 | 238 | One RFP fracture |
| | | 8 | 4.82 | 1.87 | 7.2 | 2.13 | 270 | Beam BL buckling |

Therefore, no shear crack in the slab was expected during the tests, and the integrity of the slab ensured simultaneous displacement responses in the PT frame and the GFs.

The displacements and accelerations were measured only in the direction of the table excitations. The load cells were installed on the top of the columns and outside surface of the exterior beam-to-column connections to measure PT forces. The reference frame for measuring the lateral displacement of the specimen was established outside the shaking table. The measured data included the opening of the gap at the base of the columns and the beam-to-column interfaces, the motion of PT columns with respect to the floor beam, and the axial strain in beams.

Table III lists the program used in the earthquake simulation tests. The acceleration histories of the table were components of ground motion in the 1994 Northridge and 1999 Chi-Chi earthquakes. Figure 6 shows the ground motions and response spectra that were obtained at CNP196 (Northridge Earthquake) and TCU074 (Chi-Chi Earthquake) stations. The peak ground accelerations (PGAs) of the original motions were 0.42 and 0.6$g$ for CNP196 and TCU074, respectively (Table IV). These motions were scaled to minimize the square of error between its 5% damped response spectrum and the target spectrum of IBC 2000 at periods of 0.1, 0.5, 1.0, 1.5, and 2 s. Table IV lists the resulting PGA, and Figure 6(c) and (d) presents the resulting spectra (marked as a normalized motion) along with the IBC 2000 target spectra [23].

The two acceleration scale factors in this test program accounted for (1) the size of the test specimen and (2) the earthquake intensity. The prototype was scaled as closely as possible to the requirements for a true three-story frame model according to the similitude law, which maintains the severity (i.e. stress) in both the prototype and the scaled frame during an earthquake with a particular PGA. Since the length scale factor of the three-story frame was $S_L$, the ground motion



DOI: 10.1002/eqe

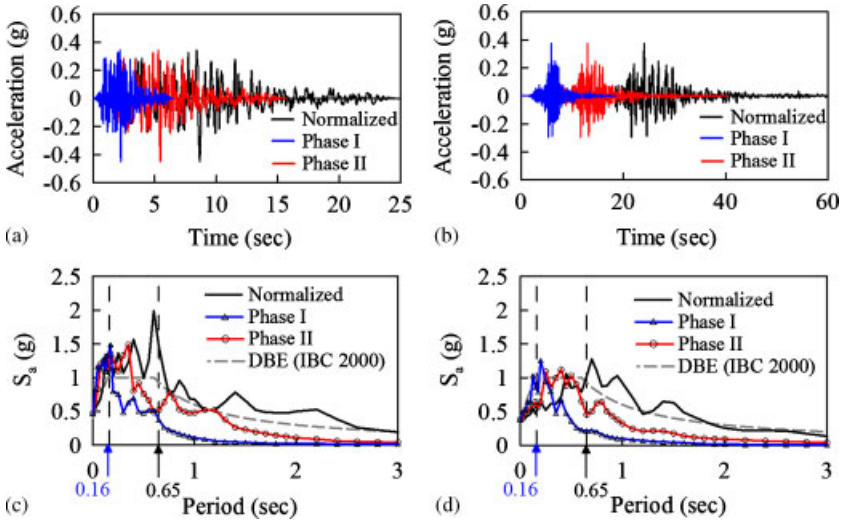


Figure 6. Ground motion and response spectra: (a) CNP196 ground motion; (b) TCU074 ground motion; (c) response spectra for CNP196 motion; and (d) response spectra for TCU074 motion.

Table IV. PGA and $S_a$ in each Phase test.

| | | | Normalized | Phase I | Phase II (time scale = 0.62) | |
|---|---|---|---|---|---|---|
| | | Original | ($T = 0.65$ s) | (time scale = 0.25, $T = 0.16$ s) | $T = 0.18$ s | $T_{eff} = 0.4$ s |
| PGA ($g$) | CNP196 | 0.42 | 0.47 | 0.47 | 0.47 | 0.47 |
| | TCU074 | 0.60 | 0.38 | 0.38 | 0.48 | 0.38 |
| Sa ($g$) | CNP196 | — | 1.45 | 1.40 | 1.32 | 0.8 |
| | TCU074 | — | 1.00 | 0.83 | 0.83 | 1.12 |

was evaluated using a time scale factor, $\sqrt{S_L}$, which was also the ratio of the period of the scaled model to that of the prototype. The fundamental periods of the prototype and the scaled one-story specimen were 0.65 and 0.16 s, respectively, so the time axis of the earthquake record was compressed by applying a scale factor of 0.25 (=0.16/0.65) to all Phase I motions. Only time was scaled to the normalized motions and the corresponding response spectra are marked as Phase I in Figure 6(c) and (d). Figure 6(c) shows that the specimen with a period of 0.16 s exhibits a spectrum acceleration, $S_a$, of 1.4$g$ (Phase I), close to that, 1.45$g$, of the prototype with a period of 0.65 s (normalized). Similarly, Figure 6(d) shows that the scaled specimen with a period of 0.16 s has an $S_a$ of 0.83$g$ (Phase I), which is slightly smaller than that, 1$g$, of the prototype with a period of 0.65 s (normalized).

Two approaches were adopted before the Phase II test to increase the displacement amplitude of the specimen. First, the seismic mass was increased from 9480 kg in Phase I to 12 640 kg in Phase II. Second, the time axis of the earthquake record was compressed by applying a scale factor of 0.62 (=0.4/0.65), where the effective period, $T_{eff} = 0.4$ s, was estimated based on the effective stiffness ($K_{eff}$) and the mass (12 640 kg) of the specimen. The effective stiffness was determined by monotonically extrapolating the hysteretic response of the specimen in Phase I test to a drift of 5% and will be presented in the following section. The period of the specimen with seismic mass of 12 640 kg was 0.18 s. Only the time axis was scaled for the normalized motions and the resulting response spectra were marked as red lines (Phase II) in Figure 6(c) and (d). Table IV shows that for the TCU074 Phase II motion, an $S_a$ value of the specimen with $T_{eff} = 0.4$ s was 1.12$g$, larger than that, 1$g$, of the prototype with a period of 0.65 s. In each test, another factor, as listed in Table III, was used to decrease/increase the earthquake intensity (PGA) of Phase I or II motion.



DOI: 10.1002/eqe

## TEST RESULTS

### *Global response*

The specimen was tested nine times in Phase I and eight times in Phase II (Table III). Figure 7 shows the relationship between the peak responses and the maximum drifts for each test. The hysteretic response was linear-elastic for a base shear of below 125 kN (Figure 7(a)). Only three Phase I tests resulted in nonlinear behaviors of the frame when PGA was larger than 0.93*g*. The Phase II tests, except for two with PGAs of 0.49 or 0.65*g* (Table III), presented nonlinear responses of the frame, indicating that the nonlinear response of the specimen was achieved by adding structural weight and re-compressing the acceleration time history. Figure 7(b) shows that the frame expansion has about a linear relationship with the drift.

After the seventh Phase I test, the initial PT force in the column CC (Figure 8(a)) decreased because the base of the column was shortened. The displacement transducer at the base of the column showed a shortening of 0.5 mm after the test (Figure 8(b)), leading to a reduction of 17 kN from the initial PT force. Minor yielding at the junction between the beam flange and web occurred during this test (Figure 8(c)). The displacement transducer at the beam-to-column interface revealed a shortening of 0.2 mm (Figure 8(b)), reducing the PT force by 8 kN from its initial value. The reduction in the PT force due to shortening was about 80–85% of that measured from the load cell, indicating that relaxation of the PT strands or seating of the strands in anchorages may be responsible for additional force losses. The shortening that was revealed by the measurements may have been caused by the conducting of many severe dynamic tests on the specimen.

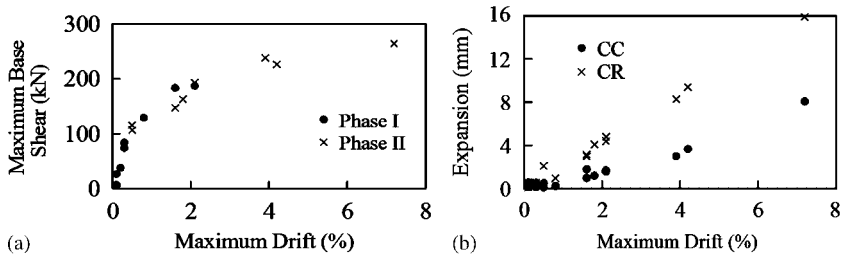


Figure 7. Maximum responses of the specimen: (a) maximum drift versus base shear and (b) maximum expansion versus maximum drift.

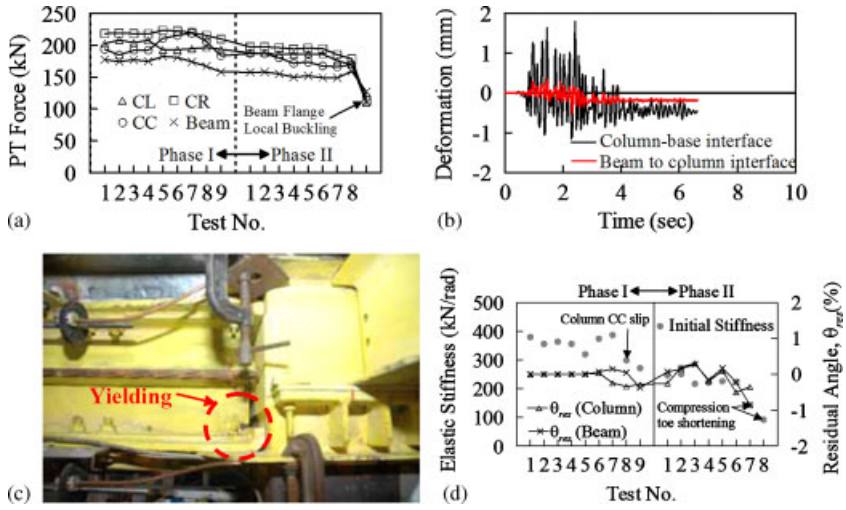


Figure 8. Variations of PT force and associated response: (a) initial post-tensioning force variation; (b) residual deformation (7th test, Phase I); (c) junction yielding (7th test, Phase I); and (d) stiffness and residual angle.



DOI: 10.1002/eqe

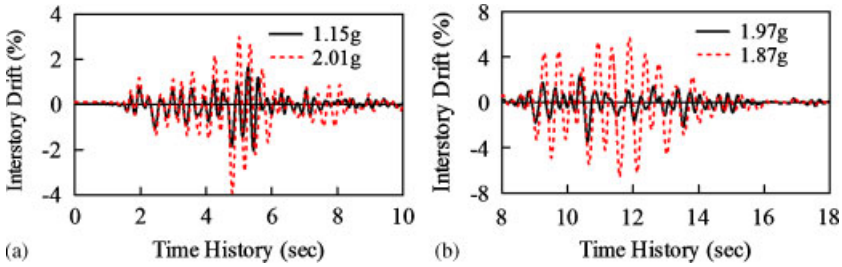


Figure 9. Displacement history response of the PT frame (Phase II): (a) CNP196 and (b) TCU074.

Figure 9(a) shows the displacement responses of the PT frame for selected PGA = 1.15 and 2.01$g$; the maximum drift increased with PGA. The PT frame reached a maximum interstory drift of 3.9% during the sixth test with PGA = 1.97$g$ (Figure 9(b)), causing the fracture of one RFP that was welded to the column CR. Fracture of the RFP was unexpected because the maximum strain in the RFP that was computed from the measured elongation was 13.6%, less than the ultimate strain (= 18.6%) determined from the coupon tensile test. The damage to the RFP was caused by cumulative inelastic strains during several tests. The bottom of the beam near the column face exhibited minor local buckling, which was not observed in beam-to-column sub-assemblage tests [1–4]. The PT frame was retested using the same record with a lower PGA = 1.87$g$. The maximum interstory drift of the PT frame was 7.2%, much larger than the 3.9% that was induced by the same ground motion of larger intensity (Figure 9(b)), indicating that the loss of RFPs or PT forces increased the interstory drift. The specimen re-centered in all of the tests because the strands in the beams and the PT bars in the columns remained elastic throughout tests.

Figure 10(a)–(c) plots the total base shear versus drift in the three tests. The base shear was defined as the total weight times the measured acceleration of the slab. The elastic stiffness $K$, indicated in these figures, was calculated based on the stiffness of the initial loading stage below 0.2% drift. No significant change was observed before the seventh test in Phase I (Figure 8(d)); the drop in elastic stiffness from 374 kN/rad (Phase I) to 224 kN/rad (Phase II) was associated with residual angles $\theta_{res}$ at the base of the column and the beam-to-column interface. The displacement transducers, which measured the gap at the base of the column CC, showed residual deformation after the seventh test; a residual angle, $\theta_{res}$, of 0.0024 rad was determined using a set of displacement transducers at the base of the column (by dividing the difference between the two measurements by the distance between them). Residual angles $\theta_{res}$ were also observed at the beam-to-column CC interface (0.0064 and 0.0015 rad from beams BR and BL to column CC, respectively). These residual angles, which were associated with partial contact of the column with the base or the beam with the column, reduced the initial stiffness of the specimen in the following test (Figure 8(d)). Buckling of the end of the beam near the column face was responsible for the significant reduction in the elastic stiffness in the eighth test (Phase II). Figure 10(d) shows the lateral deformation of the frame when it reached 7.2% drift in the last test. After all of the tests, the gravitational system remained operable and the specimen did not collapse, indicating satisfactory design performance. However, local buckling was found at the bottom of the beam near the column face, producing a permanent gap at the beam-to-column interface (Figure 10(e)). No local buckling occurred at the top of the beam. Since the beam was not composite with the slab near the column face and the slab was detailed to avoid contact with the column, the slab did not carry compressive stress in parallel with the beam flange. Because of the axial force in the beam that comprises the lateral force and the post-tensioning force, the bottom flange of beam BL is more likely to buckle than its top flange (Figure 11). When the beam bottom flange is in contact with the column in the positive direction, the axial force in the beam caused by the lateral force is compressive, adding to the compression caused by the post-tensioning force. However, when the beam top flange is in contact with the column in the negative direction, the axial force in the beam caused by the lateral force is tensile, decreasing the compression caused by the post-tensioning force. Local buckling occurred where the maximum compressive load ($F_{blr} = T_{ST} + 3F_x/4$) was expected in this floor slab system. This



DOI: 10.1002/eqe

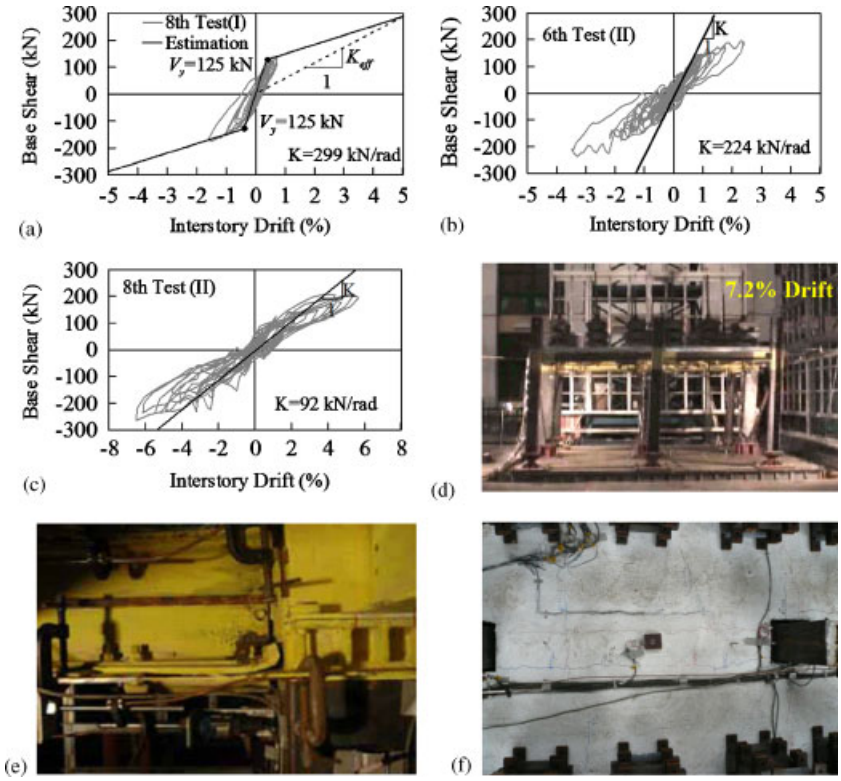


Figure 10. Force versus displacement response and observed performance: (a) 8th test (Phase I); (b) 6th test (Phase II); (c) 8th test (Phase II); (d) specimen deformation (8th test, Phase II); (e) local buckling (after 8th test, Phase II); and (f) slab crack (after 8th test, Phase II).

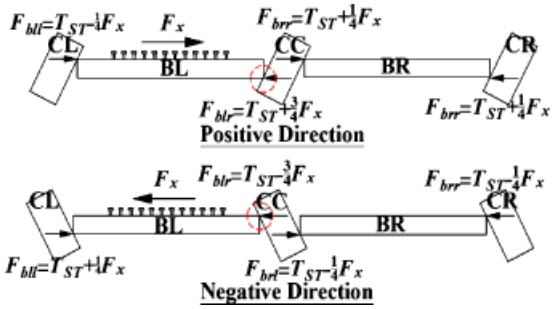


Figure 11. Force transfer mechanism.

failure mode was not expected for the beam with FRPs, designed as in prior studies [1, 2, 4, 19]. Therefore, the web and flange should be conservatively stiffened to avoid buckling.

In terms of the Phase I test, the maximum acceleration measured on the floor was 2.35$g$ under the Northridge motion, exceeding the $S_a$ values of the specimen (1.4$g$) and the prototype building (1.45$g$) for the DBE level. The maximum base shear of the specimen was 187 kN, which exceeded the yield force $V_y$ (=125 kN), determined from a significant transition in the hysteresis loops (Figure 10(a)). When the earthquake intensity in the Phase II test increased, the maximum acceleration of the floor exceeded an $S_a$ of the DBE in many tests (Tables III(b) and IV). The maximum base shear was 270 kN (=2.2$V_y$), which was about as severe as when the three-story prototype frame, was pushed to a drift of 5% (Figure 2(i)). The specimen was thus determined to have been intensely loaded in the Phase II tests.



DOI: 10.1002/eqe

The maximum base shear was 270 kN, close to the shear capacity of the slab, $V_{cr}$, at cracking (264 kN). No shear cracks were detected in the slab, but minor cracks along the edges of the top flange of the beam were found (Figure 10(f)). These longitudinal cracks were produced by vertical deformation between the PT frame, which tended to move up when the gap opened at the column base, and the GF, which did not move vertically with the pin at the base of the column. Unlike prior slab details [18, 19], which were generally cracked in a direction transverse to the PT beam at low drift and exhibited wire mesh fractures near the column at high drift, this slab retained its integrity throughout all tests and had greater serviceability.

*PT frame expansion*

Figure 12 plots the displacement histories in the PT frame (LL3), the slab (LL4), and the GF (LL5) in a specific test. The displacement histories show minor residual deformations of the specimen under the Northridge motion with floor acceleration = 2.01$g$, which exceeds an $S_a$ of the DBE (Table IV). Generally speaking, the displacement history of the PT frame is almost in phase with that of the floor slab or the GF. At 3.8 s when the specimen reached a peak lateral deformation (79 mm), lateral displacements measured by the displacement transducers LL3, LL4, and LL5 differed by 4 mm (5% difference). Chou *et al.* [17, 18] showed that when the slab provides restraints to the PT connections, the gap at the beam-to-column interface is much smaller on the beam top flange than the bottom flange. Figure 13(a) shows displacement histories measured by the transducers BG4 and BG5, which were placed near the column CC (Figure 13(b)). At 3.95 s when the beam bottom flange was in contact with the column, the displacement transducer BG4 showed a negative value (−4.1 mm). Meanwhile, the beam top flange where the displacement transducer BG5 was located also showed a negative value of −2.5 mm. At 4.13 s when the beam top flange where the displacement transducer BG5 was located was away from the column, opening measured by BG5 was 7.5 mm larger than 6.3 mm measured by BG4 at the beam bottom flange.

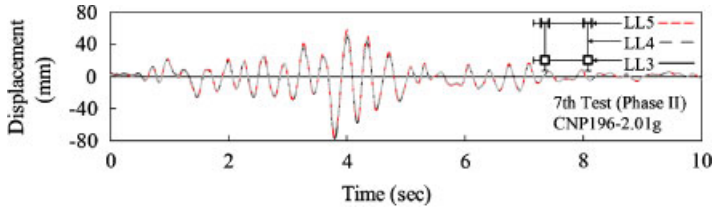


Figure 12. Displacement histories between PT and gravitational frames.

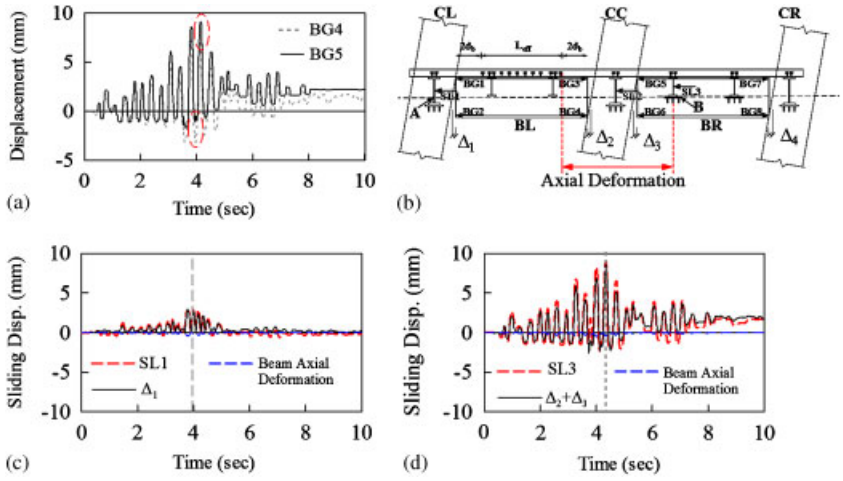


Figure 13. PT frame expansion histories (seventh test, Phase II): (a) BG4 and BG5 displacement histories; (b) displacement transducer layout; (c) floor beam A; and (d) floor beam B.



DOI: 10.1002/eqe

Although measurements were slightly different due to the shortening at 3.95 s, these data indicated that the slab restraint to the connection was minimal compared with the prior work [17]. The expansion $\Delta_1$ between column CL and beam BL was measured by a set of displacement transducers BG1 and BG2 at the beam-to-column interface (Figure 13(b)). The expansion $\Delta_1$ is close to the relative displacement between the floor beam A and the column CL (Figure 13(c)), measured by a displacement transducer SL1. Since the slab is rigidly connected to the beam BL, the expansion of column CC with respect to the floor beam B (Figure 13(b)) equals the gap:

$$\Delta_2+\Delta_3=(\mathrm{BG3}+\mathrm{BG4})/2+(\mathrm{BG5}+\mathrm{BG6})/2 \tag{6}$$

where BG3, BG4, BG5, and BG6 are the values measured by the displacement transducers placed between the center column and the beam-to-column interface. The value $\Delta_2+\Delta_3$ is close to the displacement between the beam BR and the floor beam B, measured by a displacement transducer SL3 (Figure 13(d)). It indicates that the floor slab provides minor restraints to the PT frame expansion. Beam axial deformation due to the increase in lateral force and post-tensioning force was computed by the increase in the axial force, the beam cross-sectional area, and the elastic modulus of steel. Figure 13(d) shows that the axial deformation of the beam between the rigid bay and the floor beam B (Figure 13(b)) is much smaller than the relative displacement SL3 or the gap opening displacement ($\Delta_2+\Delta_3$). The negative data in Figure 13(d) occur due to shortening of the beam bottom side in contact with the column. Note that at 3.95 s, the displacement transducers BG4 and BG5 (Figure 13(a)) had values of $-2.5$ and $-4.1$ mm due to addition of the PT force and lateral force, and opening on the beam top side was small. The data ($\Delta_2+\Delta_3$) showed a negative value during the test, indicating that the relative distance between the floor beam B and the rigid bay was shortened due to beam bearing failure near the column (Figure 10(e)). Similar response was observed in the displacement transducer SL3, but this response was minor at the beam-to-column CL interface (Figure 13(c)). Residual angles were found at the base of the column and the beam-to-column interface after the test, leading to permanent deformation between the slab and the PT beam.

*Beam axial force and column shear*

Beam instability under combined axial compression and bending is the governing limit state in design because buckling of the beam when overloaded results in loss of PT force and self-centering behavior. Figure 14 shows the free-body diagrams of the columns CL, CC, and CR at decompression. Taking the moment about a point $O_{cl}$ at the base of column CL yields the axial

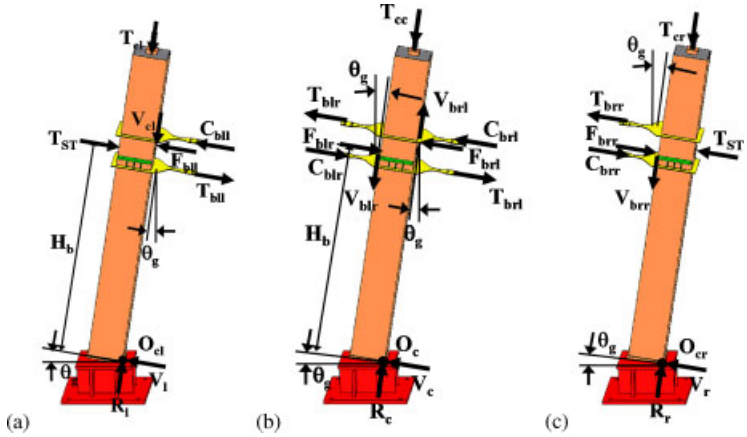


Figure 14. Column free-body diagrams (specimen model): (a) column CL; (b) column CC; and (c) column CR.



DOI: 10.1002/eqe

force on the left compression toe of the beam BL

$$F_{bll} = \frac{1}{H_b + d_{cc}}[T_{ST} H_b + T_{bll}(H_b - d_r) - C_{bll}(H_b + d_r) - T_{cl} d_c/2] \quad (7)$$

where $H_b$ is the height between the base of the column and the anchorage of the strand; $d_r$ is the distance between the centerline of the beam and the RFP; $d_c$ is the width of the column, and $d_{cc}$ is the distance between the centerline of the beam and the beam compression toe. $T_{ST}$ and $T_{cl}$ are the PT forces in the beam and column CL, which were measured by load cells. The shear force on the left compression toe of the beam BL, $V_{bll}$ is determined by considering the equilibrium of the moment about the compression toe $O_{bl}$ (Figure 15(a))

$$V_{bll} = \frac{1}{L_b}[2(F_{bll} + F_x)d_{cc} + d_r(C_{bll} + T_{blr} + C_{blr} + T_{bll}) + d_{cc}(C_{bll} + T_{blr} - C_{blr} - T_{bll}) - wL_b^2/2] \quad (8)$$

where $L_b$ is the beam length and $w$ is the uniformly distributed dead load. The shear force, $V_{blr}$, and the axial force, $F_{blr}$, on the right compression toe are determined from the equilibriums of horizontal and vertical forces in the beam BL. The axial force, $F_{brl}$, in the beam BR, which acts on the right side of column CC is obtained by using the moment equilibrium at a point $O_c$ of column CC (Figure 14(b))

$$F_{brl} = \frac{1}{H_b + d_{cc}}[F_{blr}(H_b - d_{cc}) - V_{blr} d_c - T_{cl} d_c/2 + (C_{blr} + T_{brl})(H_b - d_r) - (T_{blr} + C_{brl})(H_b + d_r)] \quad (9)$$

The shear force on the compression toe of beam BR, $V_{brl}$, is determined by considering the moment equilibrium about a compression toe $O_{br}$ (Figure 15(b))

$$V_{brl} = \frac{1}{L_b}[2F_{brl} d_{cc} + d_r(C_{brl} + T_{brr} + C_{brr} + T_{brl}) + d_{cc}(C_{brl} + T_{brr} - C_{brr} - T_{brl}) - wL_b^2/2] \quad (10)$$

The axial force and shear force on the right compression toe are determined from the equilibrium of horizontal and vertical forces in the beam BR (Figure 15(b)). Therefore, the column shears at the base, $V_l$, $V_c$, and $V_r$, can be determined based on the horizontal force equilibrium in each column.

Figure 16(a) plots the displacement history of the specimen subjected to the TCU074 record. At 10.13 s, the compressive force along the length of beam BL, given by Equation (9), is shown in Figure 16(b). Based on the assumption that the inertial force, which equaled the mass multiplied by the corresponding acceleration of the slab, was uniformly distributed to the beam BL by shear studs, the axial force in the beam BL decreased linearly from one end to the other. The interaction value (Figure 16(c)), considering the axial force and the bending moment, shows that the beam

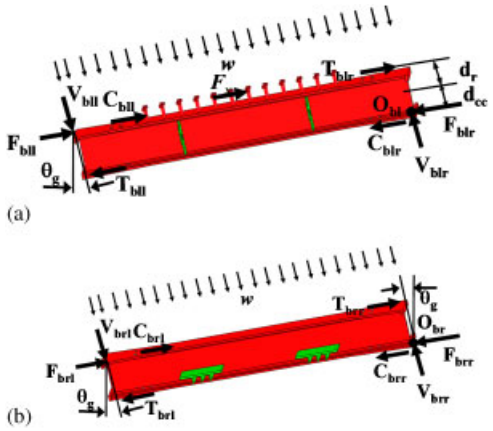


Figure 15. Beam free-body diagrams (specimen model): (a) beam BL and (b) beam BR.



DOI: 10.1002/eqe

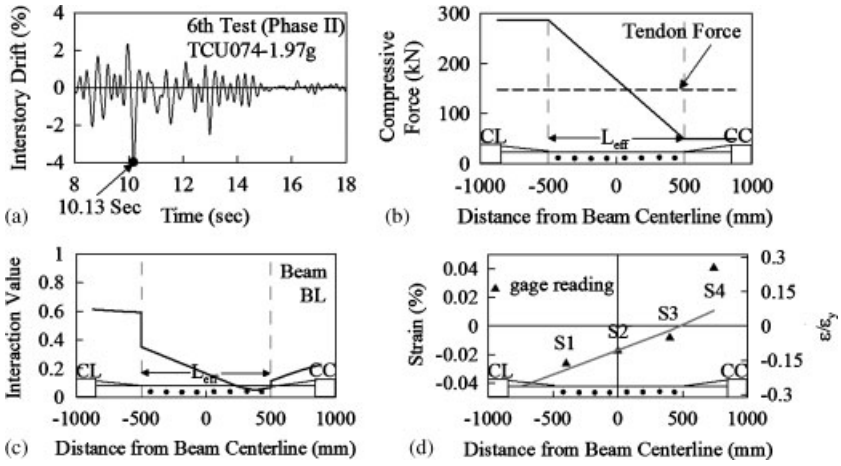


Figure 16. Axial force and strain in the beam (TCU074, sixth test, Phase II): (a) displacement history of the PT frame; (b) axial force in beam BL; (c) stress ratio in beam BL; and (d) beam BL bottom flange strain.

Table V. Column shear comparison (Phase II test).

| Test no. | 1 | 2 | 3 | 4 | 5 | 6 | 7 | 8 |
|---|---|---|---|---|---|---|---|---|
| $V_b$(kN) | 106 | 193 | 115 | 147 | 163 | 238 | 226 | 270 |
| $\frac{V_l}{V_b/4}$ | 1.01 | 1.07 | 1.03 | 1.02 | 1.00 | 0.88 | 1.15 | 1.07 |
| $\frac{V_c}{V_b/4}$ | 1.95 | 1.91 | 1.96 | 1.96 | 1.94 | 1.76 | 1.60 | 1.73 |
| $\frac{V_r}{V_b/4}$ | 0.93 | 0.91 | 0.93 | 0.94 | 1.06 | 1.36 | 1.35 | 1.20 |

remains elastic up to a drift of 4%. The flange strain calculated from the axial force and the bending moment is correlated closely with the reading from strain gauges (Figure 16(d)).

Table V lists the computed column shear for the specimen at the peak drift. The total base shear $V_b$ was computed from multiplying the measured peak acceleration with the weight. The maximum shear of the exterior column was about half that of the center column. The error in the prediction increased in the last two tests when the beam buckled and the RFP fractured.

## CONCLUSIONS

This study proposes details of a composite slab that can minimize restraints on the PT frame expansion. The slab features have (1) a rigid connection between the slab and the beam in a single bay of the PT frame, (2) roller-supported connections among the slab and the PT beams in other bays, and (3) rigid connections among the slab and the floor beams. A device is installed between the floor beams and the non-composite PT beams (i.e. beam BR) to permit sliding between the PT frame and the GFs. Many shake table tests were conducted on a two-bay by one-story building structure to examine its seismic performance. The results of the shake table test support the following conclusions:

1. The maximum inertial force in the PT frame is about double the yield force of the specimen, leading to beam bottom flange buckling, column base sliding, and RFP fractures. Losses of RFPs and PT forces significantly increase the drift from 3.9 to 7.2%. After a total of 17 shake table tests were conducted the initial post-tensioning force decreased by 50 and 22%



DOI: 10.1002/eqe

in the columns and beams, respectively, and the reduction in frame lateral stiffness was 75%. The specimen is still self-centering with a residual drift of 0.01%, which satisfies the design performance criteria. Note that the beam web and flange should be conservatively stiffened to avoid the unexpected bottom flange buckling.

2. The seismic force, transferred into the PT frame via the beam BL, causes the axial forces in the beam to exceed those in the beam BR. Although the transfer of seismic forces in the PT frame differs from that in the welded moment-resisting frame, the shear ratio between the center and exterior columns is about two.
3. As long as the shear capacity of the slab at cracking is larger than the seismic force, the displacement response of the PT frame is almost in phase with that of the GF. Splitting cracks near the column face, which were found in the prior slab details [13, 18, 19], are not found in this slab during all tests, so the slab details in this study enhance serviceability. Moreover, the frame expansion is similar to the relative displacement between the slab and the PT beam, indicating that the friction in the proposed sliding device is low and the slab can slide easily with minor restraints to the PT frame.

## ACKNOWLEDGEMENTS

This study was funded by the National Science Council, Taiwan with Professor K. C. Tsai as the Program Director. The writers are grateful to Professor Judy Liu of Purdue University for the support in this project.

## REFERENCES

1. Ricles JM, Sause R, Peng SW, Lu LW. Experimental evaluation of earthquake resistant posttensioned steel connections. *Journal of Structural Engineering* 2002; **128**(7):850–859.
2. Christopoulos C, Filiatrault A, Uang CM, Folz B. Posttensioned energy dissipating connections for moment-resisting steel frames. *Journal of Structural Engineering* 2002; **128**(9):1111–1120.
3. Rojas P, Ricles MJ, Sause R. Seismic performance of posttensioned steel moment resisting frames with friction devices. *Journal of Structural Engineering* 2005; **131**(4):529–540.
4. Chou C-C, Chen J-H, Chen Y-C, Tsai K-C. Evaluating performance of post-tensioned steel connections with strands and reduced flange plates. *Earthquake Engineering and Structural Dynamics* 2006; **35**(9):1167–1185.
5. Chou C-C, Chen YC. Cyclic tests of post-tensioned precast CFT segmental bridge columns with unbonded strands. *Earthquake Engineering and Structural Dynamics* 2006; **35**:159–175.
6. Tsai K-C, Chou C-C, Lin C-L, Chen P-C, Jhang S-J. Seismic self-centering steel beam-to-column moment connections using bolted friction devices. *Earthquake Engineering and Structural Dynamics* 2008; **37**:627–645.
7. Kim HJ, Christopoulos C. Numerical models and ductile ultimate deformation response of post-tensioned self-centering moment connections. *Earthquake Engineering and Structural Dynamics* 2008; **38**(1):1–21.
8. Chou C-C, Hsu CP. Hysteretic model development and seismic response of unbonded post-tensioned precast CFT segmental bridge columns. *Earthquake Engineering and Structural Dynamics* 2008; **37**:919–934.
9. Chou C-C, Lai Y-J. Post-tensioned self-centering moment connections with beam bottom flange energy dissipators. *Journal of Constructional Steel Research* 2009; **65**(10):1931–1941.
10. King AJ. Design of collector elements for steel self-centering moment resisting frames. *Thesis*, Purdue University, West Lafayette, IN, 2007.
11. Herning G, Garlock MM, Ricles J, Sause R, Li J. An overview of self-centering steel moment frames. *Proceedings of the Structures Congress*, Austin, TX, 2009.
12. Ricles JM, Sause R, Garlock MM, Zhao C. Posttensioned seismic-resistant connections for steel frames. *Journal of Structural Engineering* 2001; **127**(2):113–121.
13. Kim HJ, Christopoulos C. Seismic design procedure and seismic response of post-tensioned self-centering steel frames. *Earthquake Engineering and Structural Dynamics* 2008; **38**(3):355–376.
14. Garlock M, Liu J, King A. Construction details for self-centering moment resisting frame floor diaphragms. *U.S. Taiwan Workshop on Self-Centering Structural Systems*, Taipei, 2006.
15. Garlock MM, Sause R, Ricles MJ. Behavior and design of posttensioned steel frame systems. *Journal of Structural Engineering* 2007; **133**(3):389–399.
16. Chou C-C, Chen J-H. Column restraint in post-tensioned self-centering moment frames. *Earthquake Engineering and Structural Dynamics* 2010; **39**(7):751–774.
17. Chou C-C, Tsai K-C, Chen J-H, Chen Y-C, Chuang S-C. Cyclic behavior of post-tensioned steel connections with reduced flange plate and slab. *The First International Conference on Advances in Experimental Structural Engineering*, Nagoya, Japan, 2005.



DOI: 10.1002/eqe

18. Chou C-C, Wang Y-C, Chen J-H. Seismic design and behavior of post-tensioned steel connections including effects of a composite slab. *Engineering Structures* 2008; **30**:3014–3023.
19. Chou C-C, Tsai K-C, Yang W-C. Self-centering steel connections with steel bars and a discontinuous composite slab. *Earthquake Engineering and Structural Dynamics* 2009; **38**(4):403–422.
20. Chou C-C, Wu C-C. Performance evaluation of steel reduced flange plate moment connections. *Earthquake Engineering and Structural Dynamics* 2007; **36**(14):2083–2097.
21. Chou C-C, Chen JH. Tests and analyses of a full-scale post-tensioned RCS frame subassembly. *Journal of Constructional Steel Research* 2010; **66**(11):1354–1365.
22. Tsai K-C, Lin B-Z. Development of an object-oriented nonlinear static and dynamic 3D structural analysis program. *CEER/R92-04*, Center for Earthquake Engineering Research, National Taiwan University, 2003.
23. IBC 2000. International Building Code. International Code Council, Falls Church, Virginia, 2000.
24. AISC (American Institute of Steel Construction). Manual of steel construction load and resistance factor design. Chicago, IL, 2005.
25. Collins MP, Mitchell D. *Prestressed Concrete Structures*. Prentice-Hall: New Jersey, 1991.



DOI: 10.1002/eqe